Panel (d) shows the full Raman spectrum recorded at the round hole marked with the red square in Fig. 31(a). It can be compared with the spectrum (Fig. 31(h)) obtained from the hexagonal hole demarcated in blue in panel (e). As the intensity of all Raman peaks also depends on, e.g., the amount of graphene probed, laser intensity etc., it is common not to look at the absolute intensity but rather at the ratio of two peaks. Here we focus on the ratio of the D to the G peak intensity I(D)/I(G). The D peak intensity for the hexagonal hole is one order of magnitude smaller than that for the round hole (26%). The D peak intensity for regions without holes (bulk) is not zero but approximately equal to 0.02. We attribute this to some imperfections generated during the preparation of the sample. This background is also visible in the Raman map in Fig. 31(c) and 31(g). The laser beam exposes part of the bulk region, and the exposed surface represents a large fraction in comparison with the one-dimensional edge. Therefore this background should be subtracted from the measured peak intensities. Taking this into account the ratio I(D)/I(G) for the boundaries of the hexagonal holes is up to a factor of 30 smaller than for the edges of round holes. It points to a strong discrimination between the different crystallographic chiralities.

In summary, we have demonstrated that hexagonal holes obtained by anisotropic etching are bounded predominantly by zigzag edges which do not contribute to the D peak in Raman spectroscopy. Conversely, the absence of a significant D peak near such edges supports a posteriori the validity of the Raman theory which has been developed for graphene edges but could not be confirmed on the corners of mechanically exfoliated flakes. The fabrication of edges with a clean zigzag configuration represents a powerful additional capability in the graphene toolbox. It may be used as a straightforward technique to identify the crystallographic orientation of graphene flakes. By appropriate prepatterning, hexagons may be arranged so as to form constrictions or one-dimensional channels terminated on either side by pure zigzag edges. Also more advanced low-dimensional structures, such as quantum dots bound exclusively by zigzag edges, are conceivable.

[1] Research Institute for Technical Physics and Materials Science, Budapest, Hungary

Orbital reflectometry of oxide heterostructures

E. Benckiser, M.W. Haverkort, A. Fraño, O.K. Andersen, G. Cristiani, H.-U. Habermeier, A.V. Boris, I. Zegkinoglou, V. Hinkov and B. Keimer

The electronic properties of transition metal oxides (TMOs) are determined by the interplay of the spin, charge, and orbital degrees of freedom of the valence electrons. In bulk TMOs, spatial variations of the *d*-orbital occupation are known to generate a multitude of electronic phases with radically different macroscopic properties, and the influence of 'orbital reconstructions' on the physical properties of surfaces and interfaces is currently a subject of intense investigation. At present, however, only the spatial average of the orbital occupation can be determined in a facile and quantitative manner, by means of X-ray linear dichroism (XLD), a method that relies on the excitation of core electrons into the valence *d*-orbitals by linearly polarized photons. Methods used to determine site-specific variations of the orbital occupation in the bulk are mostly qualitative and/or require extensive model calculations that add substantial uncer-

tainties. Even less information is available on orbital polarization profiles near surfaces and interfaces, which are currently in the center of a large-scale research effort driven by prospects to control and ultimately design their electronic properties [1]. Since the orbital occupation determines the electronic bandwidth and the magnetic exchange interactions at and near the interfaces, detailed experimental information on the orbital polarization is essential for the design of suitable heterostructures.

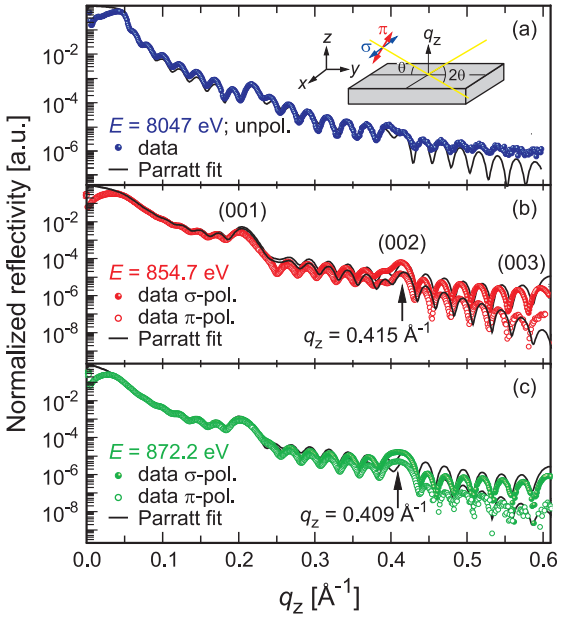

Figure 32: Momentum-dependent X-ray reflectivity of the (4 u.c. // 4 u.c.) × 8 LNO–LAO superlattice for photon energies of (a) $E = 8047$ eV (Cu K_α; hard X-rays), (b) $E = 854.7$ eV (Ni L_3), and (c) $E = 872.2$ eV (Ni L_2). All data have been normalized to 1 at $q_z = 0$. The measurements in the soft X-ray range have been performed with σ and π polarization of the incident X-rays (see sketch in (a)). The solid black line is the best fit to the data when using the Parratt algorithm. The fitted parameters, roughness and thickness, are summarized in the table below. The estimated error bars of the individual thicknesses and roughnesses are approximately ± 0.5 Å.

Here we show that it is possible to derive quantitative, spatially resolved orbital polarization profiles from soft X-ray reflectivity data, without resorting to model calculations. We demonstrate that this new method is sensitive enough to resolve differences of ≈ 3% in the occupation of Ni e_g orbitals in adjacent atomic layers of a superlattice, comprised of the paramagnetic metal $LaNiO_3$ (LNO) and the band insulator $LaAlO_3$ (LAO). The Ni^{3+} ions in LNO have a $3d^7$ electron configuration, and the nearly cubic crystal field of the perovskite structure splits the atomic $3d$ orbital manifold into a lower-lying triply-degenerate t_{2g} level occupied by six electrons and a higher-lying doubly-degenerate e_g level with a single electron. While in bulk LNO the two Ni e_g orbitals (with x^2–y^2 and $3z^2$–r^2 symmetry) are equally occupied, model calculations have suggested that the x^2–y^2 (in-plane) orbital can be stabilized by epitaxial strain and confinement in a superlattice geometry [2,3].

We have used pulsed laser deposition to grow a (4 u.c. // 4 u.c.) × 8 LNO–LAO superlattice on a $SrTiO_3$ (STO) substrate (u.c.: pseudo-cubic unit cell). The high crystalline quality and strain-state of the sample were verified by X-ray diffraction and reciprocal-space mapping. Transport and optical ellipsometry measurements in combination with low-energy muon spin rotation show that 4 u.c. thick LNO layer stacks in LNO–LAO superlattices are metallic and paramagnetic.

The reflectivity measurements in specular geometry for photon energy 8047 eV, far from resonance in the hard X-ray range reflect the high quality of the investigated superstructure (Fig. 32(a)). At energies corresponding to the Ni $L_{3,2}$ resonances at 854.7 eV and 872.2 eV, we observed superlattice peaks up to the third order, denoted by SL (00l), $l = 1, 2, 3$ in Fig. 32. To obtain a structural model of our superlattice, we fitted the q-dependent data using our newly developed reflectivity analysis program ReMagX ('X-ray magnetic reflectivity tool' www.mf.mpg.de/remagx.html).

Figure 33(a) shows the X-ray absorption spectra (XAS) measured in fluorescence-yield (FY). Due to the vicinity of the strong La M_4 white lines, the Ni L_3 line is only seen as a shoulder around 855 eV (see inset), but the Ni L_2 white line is clearly observed at 872 eV.

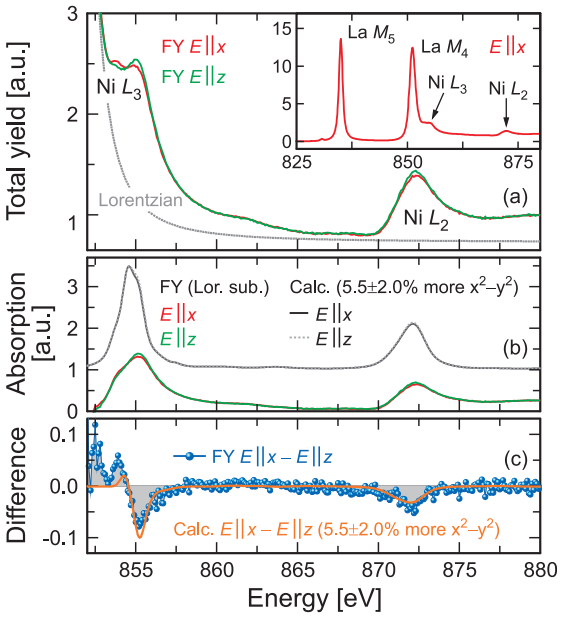

Figure 33: (a) Polarization-dependent XAS spectrum across the Ni $L_{2,3}$ edges for $E \parallel x$ (in-plane) and $E \parallel z$ (out-of-plane) polarization. In the inset the spectrum for $E \parallel x$ in the full energy range including the La $M_{4,5}$ white lines is shown. (b) Polarized spectra after substraction of a Lorentzian profile fitted to the La M_4 line shown together with results for Ni^{3+} XAS spectra with 5.5% higher x^2–y^2 occupation, obtained from the cluster calculation. (c) difference spectra ($E \parallel x - E \parallel z$) calculated from the measured (blue points) and calculated data (orange line) shown in the middle panel.

The dichroic difference spectrum, shown in Fig. 33(c), clearly shows dips at the Ni L_3 and L_2 white line energies, which we attribute to natural linear dichroism, reflecting an anisotropy of the charge distribution around the Ni ions. To obtain a quantitative estimate of the imbalance in e_g band occupation, we applied the sum rule for linear dichroism, which relates the total integrated intensity of the polarized spectra to the hole occupation. By defining the orbital polarization as

$$P = \frac{(n_{x^2-y^2} - n_{3z^2-r^2})}{(n_{x^2-y^2} + n_{3z^2-r^2})}, \qquad (7)$$

with $n_{x^2-y^2}$ and $n_{3z^2-r^2}$ being the numbers of electrons, we obtained $P = 5 \pm 2\%$. In addition we performed a cluster calculation (Fig. 33(b)), well-reproducing the observed dichroic difference for $P = 5.5 \pm 2\%$, in good agreement with the result obtained from the sum rule. While in XAS the averaged absorption of the LNO layers is measured, i.e., XAS $\propto \frac{1}{\omega}\, Im\left(f_A^{LNO} + f_B^{LNO}\right)$ for LNO layer stacks composed of two inner layers with scattering factor f_A^{LNO} and two interface layers with f_B^{LNO} (inset in Fig. 34), the intensity of the (002) superlattice reflection of a symmetric superlattice is mainly determined by the difference $F^{(002)} \propto (1 - i)\left(f_B^{LNO} - f_A^{LNO}\right)$. Taking advantage of this relation, we studied the energy dependence of the reflected intensity across the Ni L-edge for constant momentum transfers q_z in the vicinity of the (002) superlattice peak and found a pronounced polarization dependence for σ and π polarized light (Fig. 34; for the scattering geometry see the inset in Fig. 32). A qualitative comparison with the dichroic signal observed in the absorption spectra already shows a clear enhancement, which indicates a modulation of orbital occupancy *within* the LNO layer stack.

In order to confirm this conclusion and extract quantitative information about the orbital occupation, we simulated the constant-q_z scans (right panels of Fig. 34), based on the structural parameters derived from q_z-dependent reflectometry and the optical constants obtained from FY-XAS. To model the observed polarization dependence, a dielectric tensor $\hat{\varepsilon}$ of at least tetragonal symmetry has to be taken into account. Within the framework of the optical approach for multilayers, we implemented formulae derived in magnetooptics. We modeled our data with LNO layer stacks split into four unit-cell thick layers, labeled A and B in the following (inset in Fig. 34). For each layer A and B we assumed a dielectric tensor of tetragonal symmetry with complex entries ε^{ij} ($j = x,z$) related to the scattering factors f_A^{LNO} and f_B^{LNO}. In the case of a *homogeneous* LNO stack with B and A layer having the same dichroism, the measured averaged dichroism was taken as input, i.e., ε^{xx} and ε^{zz} obtained from the XAS for $E \parallel x$ and $E \parallel z$, respectively. The simulated constant-q_z scans for the *homogeneous* LNO stack cannot reproduce the large anisotropy observed in the experiment (see light blue/orange lines in the right panels of Fig. 34).

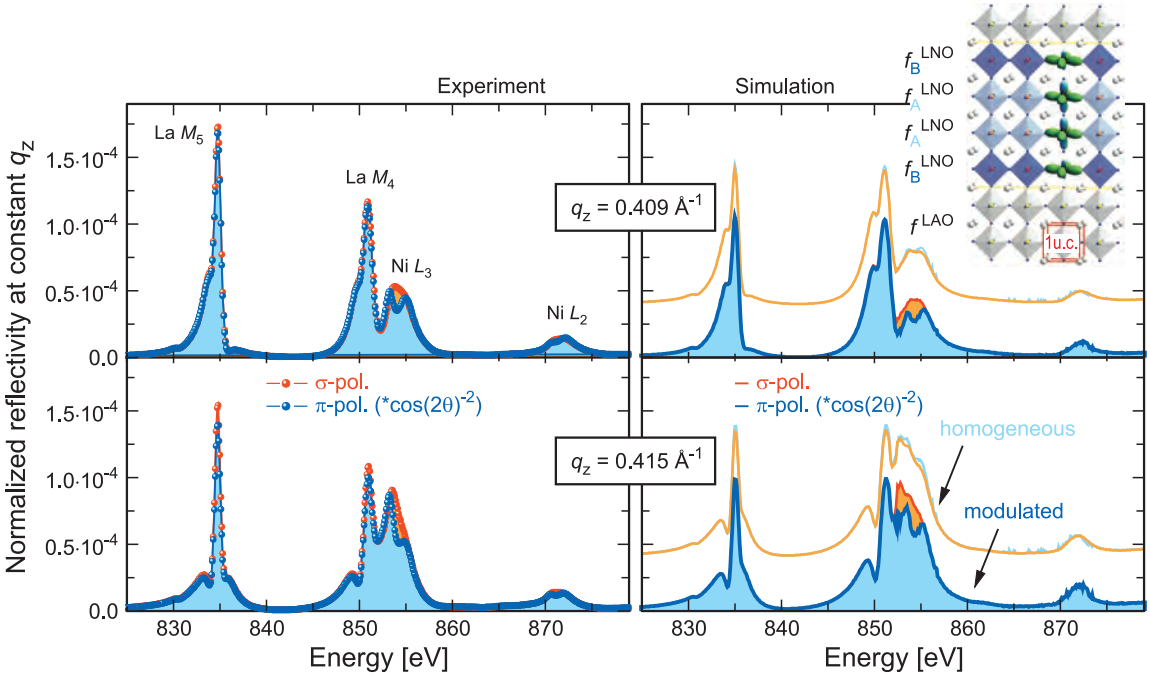

Figure 34: Energy scans of the reflectivity data with constant momentum transfer q_z at two values close to the (002) superlattice peak chosen from the q-dependent profiles (Fig. 32): $q_z = 0.409$ Å^{-1} (top panels) and $q_z = 0.415$ Å^{-1} (bottom panels). While the experimental data are shown in the left panels, in the right ones the corresponding simulated curves for LNO layers with (i) *homogeneous* orbital occupation within the LNO layer stack (shifted by 4×10^{-5} for clarity) and (ii) *modulated* orbital occupation of $P_B = 7 \pm 3\%$ higher x^2–y^2 band occupation in the interface layers and $P_A = 4 \pm 1\%$ higher x^2–y^2 band occupation in the inner layers. Experimental data and simulations are shown for σ and π polarization of the incoming photons. To correct for the difference in absolute reflected intensity for σ and π polarization due to the vicinity of the Brewster angle, we multiplied the data for π polarization with the factor $\cos(2\theta)^{-2}$ obtained by approximation from the Fresnel formulae. The inset shows a sketch of the investigated LNO–LAO superlattice with layer stacks of four pseudo-cubic unit cells (u.c., see the red box). The modulation of the Ni 3*d* e_g orbital occupation along the superlattice normal z is depicted by a different mixture of x^2–y^2 and $3z^2$–r^2 orbitals and modeled with different scattering tensor $f_{A/B}^{LNO}$ (see text). The orbital occupation imbalance has been overstated for clarity.

We therefore considered the case of a *modulated* LNO stack with different x^2–y^2 band occupation in layers A and B, keeping the averaged dichroism of $5.5 \pm 2\%$ obtained from XLD fixed. The best agreement of simulations and experiment is found for a stacking sequence BAAB with $P_B = 7 \pm 3\%$ higher x^2–y^2 population in the interface layers B and a $P_A = 4 \pm 1\%$ higher x^2–y^2 population in the inner layers A.

In order to compare our results to the predictions of ab initio electronic-structure calculations [2,3], we have performed LDA + U calculations for the particular superlattice geometry studied in this work with 4 u.c. LNO. Using equation (7), we obtain an orbital polarization of 6% (3%) for the outer (inner) NiO_2 layers B (A), in excellent agreement with the experimental result. Based on these LDA + U studies we can attribute the layer-dependent modulation of the orbital occupancy to a difference in the bonding patterns of Ni ions in inner and outer layers. Since the bonding pattern is bulk-like in the inner layers, the relatively small orbital polarization is mostly due to strain. For Ni ions in the outer layers, on the other hand, the kinetic energy-gain by out-of-plane hopping across the interface is suppressed due to the closed-shell configuration of the neighboring Al^{3+} ion and its reduced hybridization with oxygen. This explains the preferential occupation of the in-plane orbital in Ni ions adjacent to the LAO layer.

References:

[1] *Mannhart, J. and D.G. Schlom.* Science **327**, 1607–1611 (2010).

[2] *Chaloupka, J. and G. Khaliullin.* Physical Review Letters **100**, 016404 (2008).

[3] *Hansmann P., X. Yang, A. Toschi, G. Khaliullin, O.K. Andersen and K. Held.* Physical Review Letters **103**, 016401 (2009).

In collaboration with:

S. Brück (Universität Würzburg)

E. Goering, S. Macke and P. Wochner (Max-Planck-Institut für Metallforschung, Stuttgart)

X. Yang (Nanyang Technological University, Singapore)

H.-J. Kim (Daegu University, Jillyang, South Korea)

Portrait of the potential barrier at metal-organic nanocontacts

L. Vitali, G. Levita, R. Ohmann, K. Kern, A. Comisso[1] and A. De Vita[1]

Electron transport through metal-molecule contacts greatly affects the operation and performance of electronic devices based on organic semiconductors and is at the heart of molecular electronics exploiting single-molecule junctions [1]. The electronic structure at the interface between a bulk metal and an organic semiconductor thin film has been extensively studied and is commonly described in the framework of a band alignment model at the interface [2]. In the single-molecule case, however, this model faces its limits. Chemical bonding between an organic molecule and a metal surface can result in significant charge transfer and rearrangement, which depend critically on the local atomic geometry. In this situation of a strongly hybridized electronic system, a good indicator of the physical and chemical processes determining the molecule-metal contact is the work function, which for metal substrates is defined as the energy difference between the vacuum level far above the surface and the Fermi level (see also Fig. 35(a)).

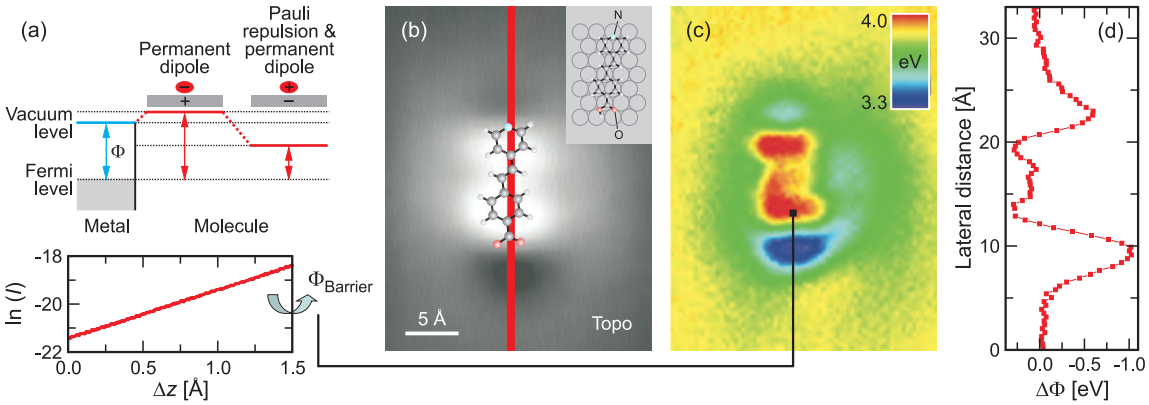

Figure 35: Potential barrier across the plane of a molecule-metal nanocontact. (a) Sketch of the work function on a clean metal (blue arrow) and at a conducting metal/organic interface (red arrow). (b) STM image of a deprotonated PVBA molecule adsorbed on Cu(111) measured in constant-current mode (–0.1 V; 0.5 nA) (inset shows a sketch of the adsorption geometry). (c) Simultaneously acquired map of the potential barrier across the molecular plane extracted from measuring the tunneling current as a function of tip-sample displacement (see bottom of (a)) at each point. (d) Work-function variation $\Delta\Phi = 2(\Phi_{Mol} - \Phi_{Cu})$ along the molecular axis.